3D Reconstruction in PET Cameras with Irregular Sampling and Depth of Interaction

P.R.G. Virador, W.W. Moses, *Senior Member, IEEE,*
R.H. Huesman, *Senior Member, IEEE,* J. Qi, *Member, IEEE*

Abstract-- **We present 3D reconstruction algorithms that address fully 3D tomographic reconstruction for a septa-less, stationary, and rectangular camera. The field of view (FOV) encompasses the entire volume enclosed by detector modules capable of measuring depth of interaction (DOI). The Filtered Backprojection based algorithms incorporate DOI, accommodate irregular sampling, and minimize interpolation in the data by defining lines of response between the measured interaction points. We use fixed-width, evenly spaced radial bins in order to use the FFT, but use irregular angular sampling to minimize the number of unnormalizable zero efficiency sinogram bins. To address persisting low efficiency bins, we perform 2D nearest neighbor radial smoothing, employ a semi-iterative procedure to estimate the unsampled data, and mash the "in plane" and the first oblique projections to reconstruct the 2D image in the 3DRP algorithm. We present artifact free, essentially spatially isotropic images of Monte Carlo data with FWHM resolutions of 1.5 mm, 2.3 mm, and 3.1 mm at the center, in the bulk, and in the corners of the FOV respectively.**

I. INTRODUCTION

W E are developing high-resolution PET cameras optimized for breast and axillary node imaging [1]. To maximize camera sensitivity, we a) pack the camera modules into a rectangular shape to minimize gaps between them, b) use the entire volume enclosed by the modules as the imaging field, and c) operate the cameras in exclusively septa-less mode. The geometry of the camera precludes motion during the scan. We therefore measure the depth of interaction (DOI) to increase the sampling rate of the camera and to reconstruct isotropic images free of artifacts, especially radial elongation. We measure the DOI by taking the ratio of the signals received by photodetectors in front and at the back of the scintillation crystals in the detector modules [2]. The DOI is measured in discrete fractions of the length of the crystals, modeling the crystals as being subdivided into 8 smaller crystals or DOI "bins."

We have previously presented results of 2D Fourier-based reconstruction methods for Monte Carlo data from a simulated camera [3], as well as 3D reconstructions based on list-mode maximimum likelihood [4]. From our 2D studies, we determined that we can nearly eliminate unnormalizable zero efficiency sinogram bins (ZEBs) and obtain isotropic

and artifact free images throughout the entire volume of the field of view by using a) small and even radial bins to exploit the high sampling rate of the camera, b) a variable-width angular binning scheme, and c) a modified filtered-backprojection technique that accommodates the irregularity in the angular sampling. In addition, we found it necessary to add a small random length to the measured DOI to make it a continuous variable, and to use the Iterative Reprojection Reconstruction (IRR) Algorithm [5] to address persisting ZEBs.

In this paper, we present the extensions of our 2D Fourier-based reconstruction algorithms into fully-3D reconstructions of Monte Carlo data from simulated cameras. Our simulation includes all of the camera's 42 modules. As in our previous paper, we present a simplified model, which we use primarily to determine the appropriate sampling parameters, and a more complete model, which includes the small gaps between modules that are due to packaging issues, realistic energy resolution in the crystals, and anticipated noise in the detector electronics.

II. POLAR ACCEPTANCE AND ANGULAR SAMPLING USING A SIMPLIFIED GEOMETRY

As in our previous paper, we employ Fourier-based reconstruction methods based on 3DRP [6] with Colsher's Filter [7]. Fig. 1 shows a diagram of the simplified camera
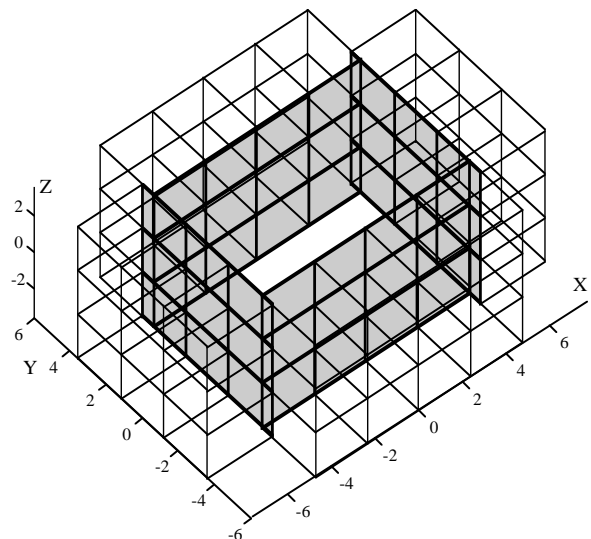

Fig. 1. Wire-frame diagram of the camera used to determine polar acceptance and angular sampling parameters. The x, y and z axes are oriented as shown. We measure the polar angle θ from the z-axis and the azimuthal angle ϕ counterclockwise from the x-axis. Units are in cm.
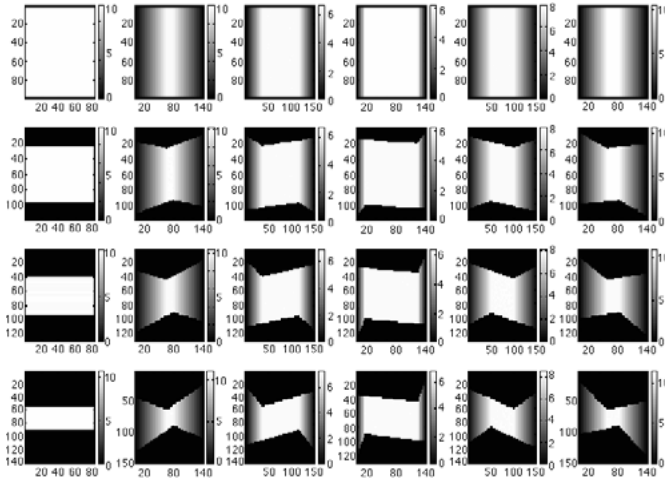
Fig. 2. Truncation pattern due to the rectangular shape of the camera. Top left is ($\theta = \pi/2$, $\phi = 0$) projection of a flood phantom. ϕ increases by 0.625 radians with each succeeding image to the right, and θ decreases by 0.125 radians with each succeeding image down. The scales vary from image to image.
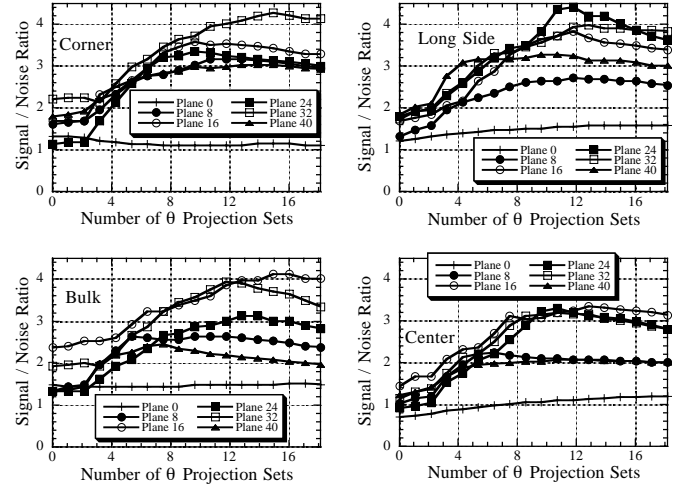

Fig. 3. SNR versus number of polar acceptance angles, used to determine the necessary polar acceptance for reconstruction. The top left, top right, bottom left, and bottom right plots are the mean SNR for voxels near the corner, along the long side, in the bulk the camera, and at the center of the camera, respectively. In each plot, the SNR from planes 0, 8, 16, 24, 32, and 40 are shown.

and describes the coordinate system that we use to determine the polar acceptance of the camera and the necessary angular sampling. Each detector module consists of 64 detector elements, each 3 mm x 3 mm x 30 mm. Fig. 2 shows projections of a flood source that fills the field of view of the camera. In many views the projections are truncated due to the limited (and unusual) polar acceptance of the camera.

A. Polar Acceptance

As the primary benefit of 3D imaging is noise reduction, we use signal-to-noise ratio (SNR) as a figure of merit to determine how much polar acceptance is necessary. We measure SNR by taking the ratio of the mean voxel value within a specified region of interest (ROI) to the variance of the voxel values within the same ROI. For this purpose, we simulate a flood phantom and calculate the mean and variance of pixels at various locations of the reconstructed image as a function of the polar acceptance. We determine the DOI by measuring the light-sharing between the PD and the PMT signals when a photon deposits energy in a crystal. The depth is determined by calculating a depth estimator Γ, defined as the ratio of the PD signal and the sum of the PD and the PMT, which varies linearly with the DOI. Γ is assumed to vary from 0.75 to 0.25 across the 30 mm crystal length. From Γ, the depth is calculated and discretized into one of eight DOI bins. Event generation and normalization are the same as discussed in [3]. The normalization data contains an order of magnitude more events than the reconstructed data.

Including DOI information, there are 172 million LORs (unique crystal segment – crystal segment combinations). Many of these LORs sample the same or nearly identical regions of the detector volume, so we rebin (based on proximity in s, θ, and ϕ) in order to reduce the data set size.

We use conservative reconstruction parameters so that we can isolate the problem of determining polar acceptance. We use coarse radial sampling of $d/2$, where d is the crystal width (3 mm), to ensure that the only unpopulated bins are those that are the result of truncation. This eliminates most

of the ZEBs that we encounter in our final algorithm, as they are the result of fine ($d/4$) radial sampling. We initially use coarse fixed-width (FW) [2] angular sampling in θ and ϕ, *i.e.* $\delta\theta = \delta\phi = 0.050$ (except $\delta\theta_{\pi/2} = \delta\phi_0 = \delta\phi_\pi = 0.075$), but later use fine FW sampling in ϕ, *i.e.* $\delta\phi = 0.025$ (except $\delta\phi_0 = \delta\phi_\pi = 0.075$) to remove the resulting streak artifacts. All angular measurements are in units of radians. We use standard 3DRP modified to accommodate the irregular sampling in both θ and ϕ. The reconstruction voxels are cubes that are 1.50 mm on a side.

We calculate the SNR in various locations of the FOV, in particular, along the short and long edges, in the corners, at the center, and in the bulk of FOV. Fig. 3 shows the SNR of the reconstructed flood phantom. The ordinate shows the SNR while the abscissa represents the number of θ projection sets used in the reconstruction, *i.e.,* an increment in the *x*-axis represents an addition of another projection set in the reconstruction as compared to the previous reconstruction. Recall that each new set of projections is $\delta\theta = 0.050$ from the previous projection. Thus, the SNR for 2D reconstruction ($\theta = \pi/2$) is the data point at $x = 1$, the reconstruction that included both the *in-plane* and the first *off-plane* events, *i.e.* at $|\theta - \pi/2| < 0.050$, is the data point at $x = 2$, the reconstruction that involves the *in-plane* events plus the events at $|\theta - \pi/2| < 0.100$ is at $x = 3$, and so on. The data point at $x = 16$ includes all the events. We use a 10x10 voxel[2] region of interest (ROI) in each of the 48 planes to calculate the SNR. Fig. 3 includes data from planes 0, 8, 16, 24, 32, and 40. Top left, top right, bottom left, and bottom right, are the SNR result for voxels near the corner, along the long side, in the bulk the camera, and at the center of the camera, respectively. The relatively flat curves are those of the bottom plane 0, which is expectedly not benefiting from additional events with more polar angles. The rest of the planes appear to benefit from more polar angle acceptance until approximately the 10th projection ($\theta = \pi/2 + 0.500$), at which point the SNR either becomes flat or begins to
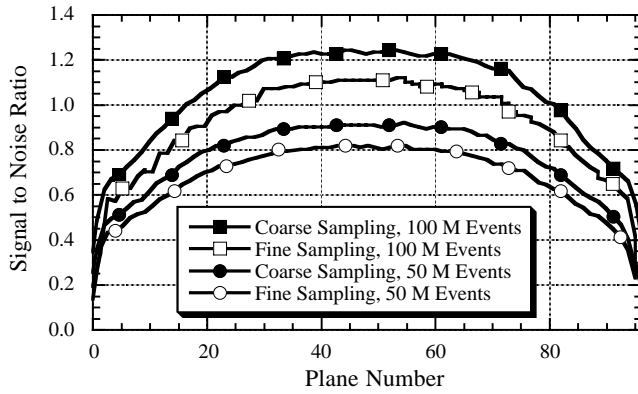
Fig. 4. Plane averaged SNR of voxels in a given plane. The squares indicate results for 100×10^6 events while the circles indicate results for 50×10^6 events. Solid symbols represent coarse polar sampling while open symbols represent fine polar sampling. The plots indicate that fine / coarse polar sampling does not greatly impact the SNR of reconstructed images.

degrade. Thus we restrict the polar acceptance to ±10 cross planes, which reduces the data set size to 68% of what it would be if we included all possible (±24) cross planes.

B. Angular Sampling

We use the same azimuthal sampling that we used in our 2D reconstruction ($\delta\phi = 0.025$), and so we only need to determine the appropriate *polar* sampling. While a higher rate of sampling results in a more accurate representation of the object being imaged, we need to weigh the cost of higher sampling in terms of larger data sets and longer reconstruction times. We therefore compare using $\delta\theta = 0.050$ and $\delta\theta = 0.025$. Because the DOI information does not increase sampling at $\pi/2$, the polar angular width $\delta\theta_{\pi/2}$ and the azimuthal angular width $\delta\phi_0$ and $\delta\phi_\pi$ are 0.075, in spite of the finer angular sampling for the rest of the azimuthal projection angles.

We again use SNR as a figure of merit to distinguish between fine and coarse polar sampling, and use the more aggressive *d/4* sampling in the following tests. This doubles the number of planes to 96 as each voxel is now a 0.75 mm cube. Fig. 4 shows the average SNR as a function of plane number for 50×10^6 and 100×10^6 events using both coarse and fine polar sampling. The results do not justify using fine sampling in the polar angle, which effectively doubles the size of the data and the reconstruction time.

We determine whether the polar sampling rate affects the resolution of reconstructed point sources. We simulate point sources in various locations of the FOV and measure their FWHM and FWTM. The measured resolutions of point sources sampled with fine polar sampling do not differ from those of point sources sampled with course polar sampling. The conclusion of these two tests is that we sacrifice neither resolution nor image quality by coarsely sampling the polar angle, *i.e.* using $\delta\theta = 0.050$. Our final sampling choices ($\delta s = 0.75$ mm, $\delta\theta = 0.050$, $\delta\phi = 0.025$, ±10 cross planes) yield a data set size of 40 million bins.

C. Sample Reconstruction

Fig. 5 shows a sample reconstruction of a tube of constant activity. We show four planes of the FOV, from the bottom
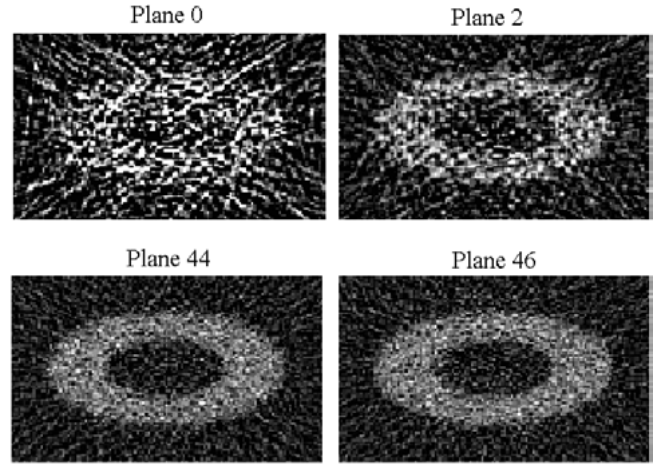

Fig. 5. Reconstruction of a tube of constant activity in a cool background. In the upper row are planes at the axial limit of the camera, in the lower row are planes near the camera center. The phantom is easily discernable except at the extreme plane.

plane to midway up the FOV. We simulate 5×10^7 annihilations in both the cold background and hot ellipse, and use a flood phantom of 5×10^9 events to normalize. While the resolution is isotropic throughout the entire FOV, these results indicate that the decreased sensitivity reduces the signal to noise ratio for planes near the axial edge of the field of view. The ellipse in Plane 0 is hard to discern and noise blurs the boundary of the ellipse in Plane 2.

Fig. 6 shows the statistics of the reconstructions in Fig. 5. The expected ratio of the mean voxel value between the source and the background is 1:4.76. While the mean voxel value within the phantom is uniform, the planes near the top and the bottom of the FOV exhibit an underestimation in the colder background, resulting in an artificially elevated ratio at the extreme planes. The magnitude of this effect decreases as the number of events used for normalization increases.
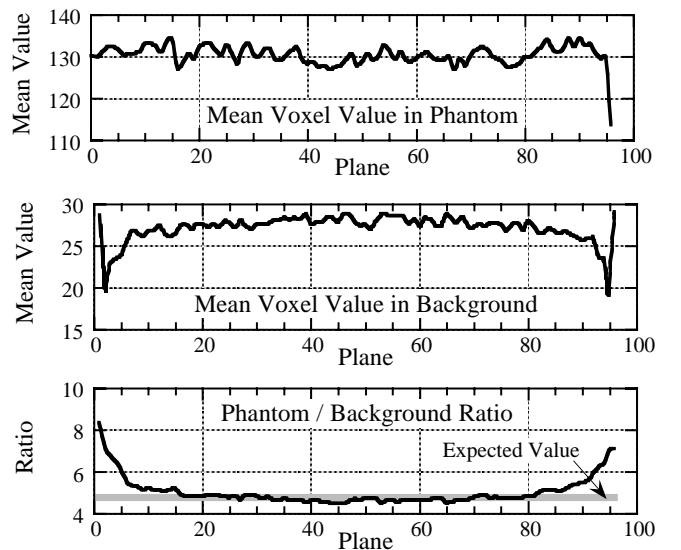

Fig. 6. Statistics of the sample reconstruction in Fig. 5. Shown are the mean voxel values of the phantom and the background as a function of the plane number. The expected ratio of the phantom activity to the background activity is shown as the straight line in the bottom plot. The apparent structure at the extreme planes is due to simplified normalization and underestimation of the detected events in these planes.
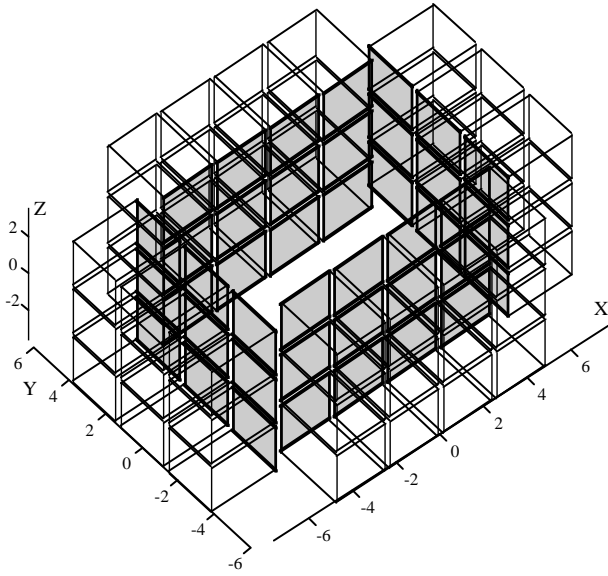
Fig. 7. Wire frame diagram of the realistic camera. The gaps between the modules, which are due to packing issues, are readily seen. These gaps result in more ZEBs in the projections, which need special attention for artifact-free reconstructions.

III. REALISTIC CAMERA

A. Simulation

Fig. 7 shows the geometry as we expect the camera to be constructed. The one crystal wide gaps between the modules are due to packing issues. As in the case of the 2D reconstructions that we have discussed in our previous paper, these gaps introduce a complication in the reconstruction in that they are an additional source of ZEBs. The gaps also result in the loss of approximately 1/3 of the events due to the loss of active detector area.

We add more realistic effects in the current simulation. Among these effects are Compton scatter in the detector modules and noise in both the photodiode and the PMT. The accepted energy window is $370\,keV < E < 650\,keV$, which has a 70% singles efficiency. The total efficiency of the simulated detector for a uniform flood source is 9%. The PD and PMT signals include noise contributions similar to those observed in prototype detector modules [2], resulting in 5–10 mm FWHM DOI measurement resolution. Because the measured DOI is the ratio of noisy signals in the photodetectors, it is possible to "measure" events whose DOI are outside the physical limits of the crystal. Such events are assigned a depth of 0 or the length of the crystal, depending of whether the calculate length is less than 0 or longer than the crystal length, respectively.

Fig. 8 shows the projections of a simulated flood phantom as observed by the realistic camera, similar to those shown for an ideal camera in Fig. 2. The directions of the projections are the same are in Fig. 2. The gaps between the modules are evident in the large contiguous unsampled regions in the projection planes. The close-spaced horizontal bands in the top row are due to the assignment of the interaction point to the center of the long axis of the crystal. Note that there are ZEBs in virtually all projections.
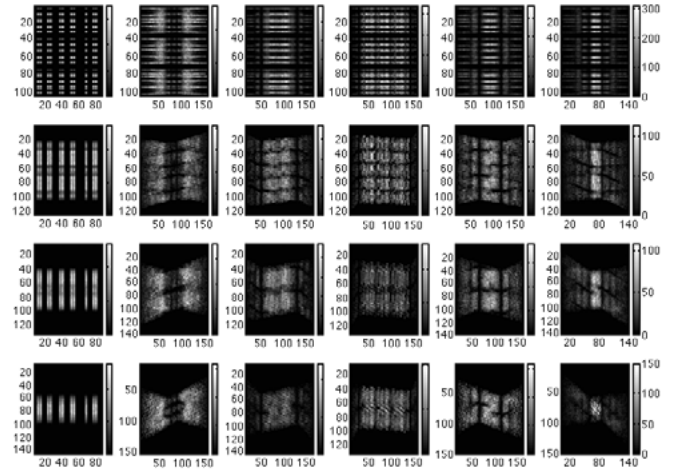

Fig. 8. Projections of a flood phantom using a simulation of the more realistic camera. Note the increase in the number of ZEBs. The projection directions corresponding to the different plots are the same as in Fig. 2.

B. Reconstructions and Results

The general approach that we take is to arrange our sampling to minimize ZEBs and use IRR and reprojection to estimate the data in the remaining unsampled (or poorly sampled, as determined by the normalization) projection bins. Thus, we first need to reconstruct the direct cross-plane data sets (which we did in [3]), forward project this initial reconstruction to fill in the unsampled bins, then reconstruct the now complete data using Colsher's filter.

Using d/4 sampling and defining interaction points to be along the long axis of the crystal leave every fourth plane of the FOV (at $\theta = \pi/2$) unsampled. To address these ZEBs, we perform angular mashing between the *in-plane* events and the first *off-plane* events. This is similar to the combination of 2D projections taken at different angles as was done with the clam motion for the LBL PET600 camera [8]. Note that if angular mashing is not performed, these unpopulated planes will remain unfilled during the 2D reconstruction that produces the initial estimate of the object in the FOV. The IRR algorithm will thus fail for these planes.

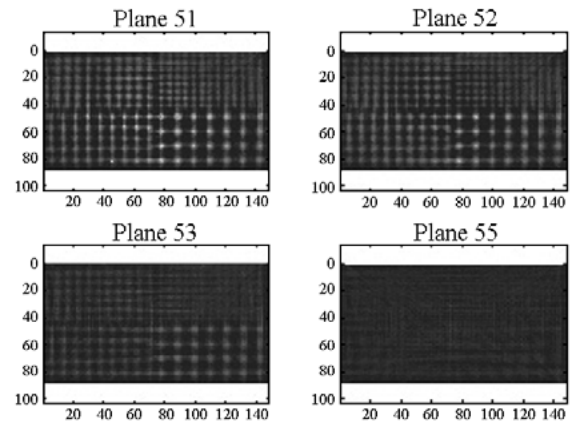Once the unsampled planes are estimated, we perform IRR

Fig. 9. Simulated sphere sources located at a central plane (plane 51). The spheres are arranged where the distances between the sources are four times their diameters (like a Derenzo Phantom). The diameters are 1.0 mm, 1.25 mm, 1.5 mm, and 2.0 mm.

Table 1. FWHM of point sources in various locations. The center column contains the values for planes near the center of the FOV while the right hand plot contains values for planes near the top and the bottom of the FOV (3.6 cm from the central plane). Values have 0.75 mm uncertainty.

(X,Y) Location (cm)	PSF FWHM (FOV Center)	PSF FWHM (FOV Edge)
(0.0, 0.0)	1.54 mm	1.91 mm
(5.4, 0.0)	2.50 mm	2.60 mm
(2.7, 1.6)	2.14 mm	2.45 mm
(0.0, 3.2)	2.63 mm	3.10 mm
(5.4, 3.2)	3.10 mm	3.18 mm

to estimate the rest of the ZEBs in the *in-plane* projections. Our simulations show that approximately 5 iterations of IRR with the positivity constraint are required before convergence is attained. We determine this by comparing the current projections with the subsequent projections after the application of IRR.

Fig. 9 shows the reconstruction of a simulated Derenzo-like resolution phantom in the near the central plane of the FOV. Top right, top left, bottom left, and bottom right quadrants are filled with 1.00 mm, 1.25 mm, 1.50 mm, and 2.00 mm diameter spheres respectively. The sphere sources are arranged so that the distances between their centers are four times their diameters. The "point sources" can easily be distinguished from each other, even the small sources that are near the periphery of the plane. If the same pattern is simulated near the top or the bottom of the camera, however, only the larger sources near the center of the plane are easily recognizable. Table 1 shows the resolutions of point sources at various locations within the FOV for planes near the center and close to the bottom and the top.

We also simulate a Defrise Phantom in the FOV. The bottom left quadrant of the FOV is filled with six 6.0 mm alternating planes of constant and no activity. The reconstruction is shown in Fig. 10. Shown are progressive 0.75 mm slices perpendicular to the *x* axis, starting from the camera center (shown in top left) and ending at the rightmost

edge of the camera (bottom right). The individual planes are readily seen and are uniform over nearly the entire camera volume. Increased noise is observed in slice 145, which is at the extreme edge (in the x- direction) of the camera. However, the noise is confined to the region near plane 0, which is the axial edge of the camera where the acceptance (and thus number of events in the image) is low.

IV. CONCLUSIONS

In conclusion, we have developed fully 3D reconstruction procedures for data from a PET camera with irregular sampling and depth of interaction measurement capability. We use evenly spaced 0.75 mm radial bins in the projection data to exploit the high sampling rate of the camera as well as to take advantage of fast and standard Fourier-based reconstruction algorithms. We modify the standard 3D reconstruction algorithm to accommodate the irregular angular sampling. To address the ZEBs that result in the discretization of the DOI, we add a small random number to the measured DOI to make it approximate a continuous variable. We address the rest of the ZEBs that are due to gaps between modules by using the IRR algorithm that estimates the missing information using *a priori* information from the object. The reconstructed point sources and extended phantoms are artifact-free. The point sources are essentially isotropic and have FWHMs that vary from 1.50 mm to 3.0 mm depending on its location in the FOV. We do not observe the adverse effects of radial elongation in the images.

V. ACKNOWLEDGMENT

VI. REFERENCES

[1] Moses WW, Budinger TF, Huesman RH, *et al.*, "PET camera designs for imaging breast cancer and axillary node involvement," *J. Nucl. Med.* 36, p. 69, May 1995.

[2] Huber JS, Moses WW, Derenzo SE, *et al.* "Characterization of a 64 channel PET detector using photodiodes for crystal identification," *IEEE Trans. Nucl. Sci.* NS-44, pp. 1197–1201, June 1997.

[3] Virador PRG, Moses WW, Huesman RH, "Reconstruction in PET cameras with irregular sampling and depth of interaction capability," *IEEE Trans. Nucl. Sci.* NS-45, pp. 1225–1230, June 1998.

[4] Huesman RH, Klein GJ, and Moses WW, "List mode maximum likelihood reconstruction applied to positron emission mammography," *IEEE Trans. Med. Img.* 19, pp. 532–537, May 2000.

[5] Medoff BP, Brody WR, Nassi A, Macovski A, "Iterative convolution backprojection algorithms for image reconstruction from limited data," *J. Opt. Soc. Am.* 73-11, pp. 1493–1500, Nov. 1983.

[6] Kinihan PE, Rogers JG, "Analytic 3D image reconstruction using all detected events," *IEEE Trans. Nucl. Sci.* NS-36, pp. 964–968, 1989.

[7] Colsher JG, "Fully three-dimensional emission tomography," *Phys. Med. Bio.* 25-1, pp. 103–115, Jan. 1980.

[8] Derenzo SE, Huesman RH, Cahoon JL, *et al.* "A positron tomograph with 600 BGO crystals and 2.6 mm resolution," *IEEE Trans. Nucl. Sci.* NS-35, pp. 659–664, Feb. 1988.
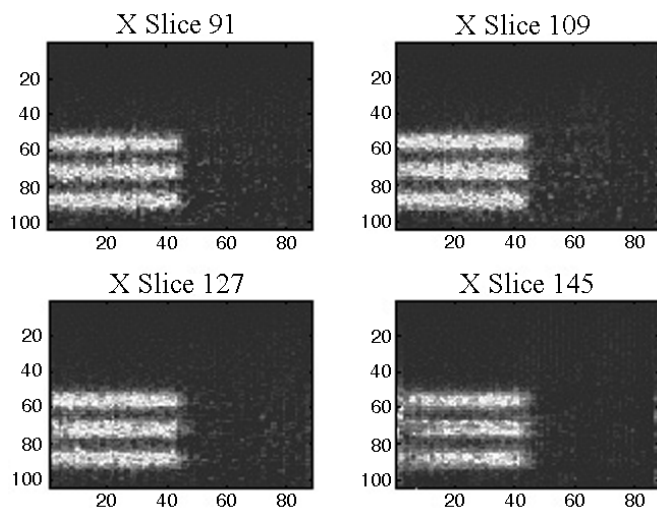
Fig. 10. Simulated Defrise Phantom. The bottom left quadrant of the FOV is filled with 6 alternating planes (6.0 mm thick) of constant and no activity. Upper left image is a plane near the camera center, lower right is at the axial edge.